Applied Catalysis B: Environmental 284 (2021) 119702

Contents lists available at ScienceDirect

Applied Catalysis B: Environmental

journal homepage: www.elsevier.com/locate/apcatb

Supported Fe_2C catalysts originated from Fe_2N phase and active for Fischer-Tropsch synthesis

Xin-Pu Fu [a], Wen-Zhu Yu [a], Chao Ma [e], Jun Lin [b], Shi-Qi Sun [b], Shan-Qing Li [d], Pu-Ning Ren [a], Feng-Yan Jia [a], Meng-Yuan Li [a], Wei-Wei Wang [a], Xu Wang [b], Chun-Jiang Jia [a,*], Ke Wu [c], Rui Si [b,*], Chun-Hua Yan [c,*]

[a] *Key Laboratory for Colloid and Interface Chemistry, Key Laboratory of Special Aggregated Materials, School of Chemistry and Chemical Engineering, Shandong University, Jinan, 250100, China*

[b] *Shanghai Synchrotron Radiation Facility, Shanghai Institute of Applied Physics, Chinese Academy of Sciences, Shanghai, 201204, China*

[c] *Beijing National Laboratory for Molecule Sciences, State Key Lab of Rare Earth Materials Chemistry and Applications, PKU-HKU Joint Lab in Rare Earth Materials and Bioinorganic Chemistry, Peking University, Beijing, 100871, China*

[d] *Department of Chemistry and Materials Engineering, Chizhou University, Chizhou, 247000, China*

[e] *College of Materials Science and Engineering, Hunan University, Changsha, 410082, China*

ARTICLE INFO

Keywords:
Fischer-Tropsch synthesis
Iron nitrides
Iron carbides
Structure-reactivity relationship
Mössbauer spectra

ABSTRACT

Fischer-Tropsch synthesis (FTS) targeting liquid fuel products is key technology to alleviate the excessive dependence on unsustainable crude oil. Fabrication of highly active phase has long been an attractive topic in the field of Fischer-Tropsch catalysis. However, as a promising active species, the efficient formation of Fe_2C phase is inhibited by kinetic barrier *via* traditional approaches. In this context, we firstly synthesized phase-pure Fe_2N nanoparticles on Al_2O_3, which has similar coordination structure with Fe_2C. The *in-situ* XRD data in time series reveal that pre-existing of interstitial N atoms in Fe_2N structure leads to the effective phase transformation to Fe_2C at low temperatures (280 °C). The as-prepared catalysts demonstrated highly catalytic activity without any induction period, coupling with a high selectivity of 60wt.% for desired valuable products. In addition, the corresponding structural evolution uncover the determining effect of these electron-rich Fe sites in the Fe_2X (N or C) structure on superior performance.

1. Introduction

Carbon based fuel will still occupy a dominate situation in the world energy market in the future. CO hydrogenation *via* Fischer-Tropsch synthesis (FTS) plays a key role in sustainably producing liquid fuel or lower olefins from non-petroleum carbon sources, such as coal, natural gas and biomass [1–11], through which desired hydrocarbons are formed through CO dissociation and C—C coupling with the help of catalysts. On account of the low price, tuneable reaction condition and excellent selectivity, iron-based catalysts have always drawn major interests for converting syn-gas to targeted hydrocarbons [12–18].

During a typical FTS reaction, complex mixtures of iron species in the catalysts are always formed, including metallic iron, iron oxides and carbidic iron. It is generally recognized that the active phases of iron-based catalysts for the FT reaction are iron carbides, including χ-Fe_5C_2, θ-Fe_3C, ε-$Fe_{2(.2)}C$, and Fe_7C_3 [18–24]. In some report, metallic iron is also acknowledged as active species owing to its ability to dissociate and hydrogenated CO as well [25,26]. Typically, iron carbides are classified according to the position of interstitial carbon atoms in the hexagonally close packed (hcp) structure of metallic iron lattice. For χ-Fe_5C_2 and θ-Fe_3C, the carbon atoms occupied the trigonal prismatic (TP) interstices with different organizations [27]. However, in general knowledge, these two kinds of TP carbides play different roles in FTS reaction, which the χ-Fe_5C_2 is normally regarded as active phase [18,19], but the θ-Fe_3C is verified as spectator to catalytic process as revealed in many reports [28]. By using a wet chemical route, Ma and co-workers synthesized Fe_5C_2nanoparticle by inducing bromide into preparation process [19], and as-prepared Fe_5C_2 nanoparticles performed highly initial activity without any induction period, which clearly proving its intrinsically active feature in catalysing FTS reaction. Highly dispersed χ-Fe_5C_2 with 86 % purity was also achieved mediated by metal organic framework in Santos's group [29]. Subsequently, the

---

* Corresponding authors.
E-mail addresses: jiacj@sdu.edu.cn (C.-J. Jia), sirui@sinap.ac.cn (R. Si), yan@pku.edu.cn (C.-H. Yan).

https://doi.org/10.1016/j.apcatb.2020.119702
Received 20 June 2020; Received in revised form 30 September 2020; Accepted 24 October 2020

pure χ-Fe_5C_2 particles were also proven as intrinsic active species for FTS reaction.

As the other kind of carbide, Fe_2C, it was theoretically predicted to has the lowest barriers for C—O dissociation and C—C coupling among various iron carbides [30,31]. However, the authentic illustration of its real role in FTS reaction was still limited by the difficulty in its direct formation. De Smit and co-workers found the phase transformation of carbide phases evolved as a function of the carbon chemical potential (μ_c). Correspondingly, the formation of Fe_2C was only favoured in high μ_c, indicating that low temperature and high CO pressure were required. However, the carbon diffusion is kinetically unfavourable under low temperature. At elevated temperature, the iron carbides were considered unstable with transforming into χ-Fe_5C_2 during the FTS reaction, which correspondingly might inhibit its presence in large amount [30]. Even so, attracted by its promising potential, inspiring efforts were made by researchers in rational design of Fe_2C catalysts [20,23,32]. For example, mediated by rapidly quenched (RQ) iron species, Xu et al. subtly synthesized carbide dominated catalyst owing to the coordinatively unsaturated microstructure of RQ iron, which demonstrated high FTS activity at 200 °C in batched reactor [20]. Wang et al. recently synthesized phase-pure ε(′)-Fe_2C by carefully controlling the pre-treatment and carburization condition [23]. These advancements reveal that it is challenging and desirable to develop a facile and feasible strategy of fabricating supported Fe_2C dominated material as an active catalyst for FTS reaction.

For another series of iron phase, iron nitrides have long been found by Anderson and co-workers as promising catalyst over FTS reaction [33,34]. Yeh et al. found the nitrogen atoms in supported Fe_2N could slowly exchange with carbon atoms under syn-gas environment [35,36]. Studies of Deglass et al. indicated the catalytic performance might be strongly influenced by the initial difference of various nitrides, including γ′-Fe_4N, ε-Fe_xN ($2 < x < 3$), and ζ-Fe_2N [37]. As one kind of these iron nitrides, the hexagonal Fe_2N have comparable positions of interstitial N atoms with the C atoms in Fe_2C basing on first-principles electronic band structure calculations [38]. These interstitial N atoms obviously expand the Fe—Fe coordination distance [39], which potentially promote the carbon diffusion and substitute N atoms with formation of Fe_2C phase. In addition, previous findings also confirmed the presence of N/C atoms exchange during FTS reaction [14,35–37]. These experimental proof and forecast basing on DFT calculation inspired us to fabricate $Fe_{2(.2)}C$ nanoparticles by using Fe_2N as phase precursor. On the other hand, it is also desirable to dig out where the intrinsic activity of Fe_2C stemmed from through monitoring its structural evolution under reaction condition.

Therefore, in this work, phase-pure Fe_2N nanoparticles supported on mesoporous Al_2O_3 were firstly synthesized with optimized condition. On account of the effective substitution between dissociated C atoms and interstitial N atoms in as-prepared Fe_2N nanoparticle, Fe_2C dominant catalyst was subsequently formed under FTS reaction condition. Benefitting from the preservation of active Fe_2X (X = N or C) structure during N/C exchanging stage, the as prepared Fe_2N/Al_2O_3 catalyst demonstrated highly initial reactivity. Results of structural evolution reveal that the electron-rich surface and superior sorption feature of Fe_2X/Al_2O_3 catalyst result in enhanced FTS activity and as well as the satisfying selectivity for desired C_2—C_4 olefin and liquid fuel products (60 wt.% in total).

2. Experimental

2.1. Preparation of support materials

Mesoporous Al_2O_3 material was firstly prepared by one soft-template method based on evaporation-induced self-assembly procedure. 1.0 g of Pluronic P123 ($M_{av} = 5800$, $EO_{20}PO_{70}EO_{20}$, Sigma-Aldrich) was dissolved in 20 mL ethanol at room temperature (RT) firstly in a typical synthesis. Afterward, citric acid (0.84 g, Tianjin BoDi Chemicals) and appropriate quantities of $Al(NO_3)_3 \cdot 9H_2O$ salts were added to the solution with vigorous stirring. These mixtures were stirred at RT for 5 h and then dried at oven at 60 °C for another 2 days. With inside a furnace, as-obtained substance was further calcined in air at 500 °C for 4 h.

2.2. Preparation of Fe_2N/Al_2O_3

1 g of as-prepared mesoporous Al_2O_3 coupled with appropriate quantities (Fe/Al equal to 15/85) of $Fe(NO_3)_3 \cdot 9H_2O$ were fully dispersed in 80 mL deionized water by ultra-sonication for 0.5 h. Following with the suspension was stirred for 1 h at RT, the mixture was heated at 353 K under vigorous stirring, and then ultimately came into being slurry liquid. With inside a furnace, the as-obtained product was dried for 10 h inside oven and subsequently calcined in air at 500 °C for 4 h. The Fe_2N/Al_2O_3 catalyst was prepared by further calcined with inside a tube furnace in ammonia atmosphere at 650 °C for another 4 h with a ramping rate of 1 °C/min. The flow rate of ammonia was tuned with a gaseous hourly space veolicity (GHSV) of 15,000 $mL \cdot g^{-1} \cdot h^{-1}$.

2.3. Preparation of the Fe_2O_3/Al_2O_3-IM and Fe_2O_3/Al_2O_3-SG as reference catalysts

The Fe_2O_3/Al_2O_3-IM was prepared in the same way with Fe_2N/Al_2O_3 without further nitridation process. The Fe_2O_3/Al_2O_3-SG catalyst was prepared by sol-gel (SG) method based on evaporation induced self-assembly path mentioned above. Appropriate $Al(NO_3)_3 \cdot 9H_2O$ and $Fe(NO_3)_3 \cdot 9H_2O$ salts (total 40 mmol, Fe/Al = 50/50) were added to the solution.

2.4. X-ray diffraction (XRD)

The *ex-situ* XRD tests were carried out on a PANalytical B.V.X'pert3 powder diffractometer with current of 40 kV and 40 mA, using Cu Kα radiation (λ = 0.15418 nm). With an acquisition time of 20 min or 3.5 h, the XRD patterns under *ex-situ* mode were collected at room temperature (RT). The *in-situ* XRD patterns were obtained from the same machine with an Anton Paar XRK-900 reaction chamber. Samples were loaded in a ceramic sample holder with diameter of 10 mm, and depth of 1 mm, and then treated with various conditions. Three rounds of measurements with each lasting for 20 min were carried out for each selected temperature. The third round of measurement was collected and used to determine the structure of the catalysts. For H_2 or CO feed, the 5 % H_2 or CO diluted by argon was used and the temperatures reached at each point with a ramping rate of 10 °C/min. For the ambient pressure test, 50 %H_2/50 %CO feed with a flow rate of 30 mL/min was used, and the patterns were firstly collected at 280 °C for 4.5 h, then increased to 330 °C for another 4.5 h and finally decreased to 280 °C again.

2.5. Transmission electron microscopy (TEM)

The TEM and high-resolution TEM (HRTEM) were conducted on a Philips Tecnai F20 instrument operating at 200 kV. The aberration-corrected HRTEM images and STEM images with the corresponding electron energy loss spectroscopy (EELS) measurements were performed on JEOL ARM200F microscope equipped with probe-forming spherical-aberration corrector and Gatan image filter (Quantum 965).

2.6. X-ray photoelectron spectroscopy (XPS)

XPS characterization was carried out on an Axis Ultra XPS spectrometer (Kratos, U.K.) with 225 W of Al K_α radiations, and with the C *1s* peak at 284.8 eV as an internal standard for all the spectra.

2.7. Temperature programmed measurements

The temperature-programmed reduction tests of H_2 (H_2-TPR) and CO

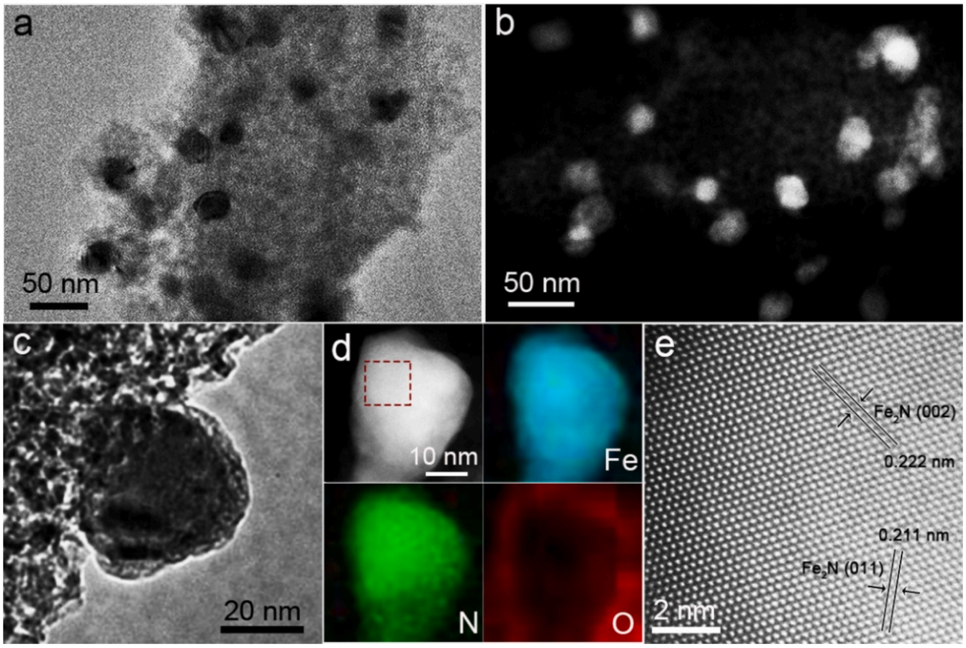

Fig. 1. Structural information of the fresh Fe_2N/Al_2O_3 catalyst. (**a**) An overview TEM image, (**b**) High Angle Annular dark-field (HAADF) STEM image, (**c**) TEM image of a single particle, (**d**) aberration-corrected (AC) STEM-EELS mapping results and (**e**) HRTEM image of as-prepared supported Fe_2N nanoparticles.

(CO-TPR) were performed in apparatus equipped with six-way valve for avoiding dead volume and residual air. The end gas was online monitored by one mass spectrometer in real-time. Before all the measurements, the Fe_2O_3/Al_2O_3 was pre-treated in pure O_2 at 300 °C for 0.5 h and the Fe_2N/Al_2O_3 was pre-treated in pure N_2 at 100 °C for 0.5 h. Under the atmosphere of 5% H_2/Ar or 2% CO/N_2, the temperature was increased from RT to 800 °C with a ramping rate of 10 °C min^{-1}. For temperature programmed desorption measurements of CO or CO_2 (CO-TPD or CO_2-TPD), the Fe_2O_3/Al_2O_3 was reduced in a flow of 5% H_2/Ar at 380 °C for 3 h and the Fe_2N/Al_2O_3 was pre-treated in pure N_2 for 0.5 h. Then CO or CO_2 was adsorbed with a flow rate of 30 mL/min at RT for 1 h and subsequently purged with pure He (30 mL/min) for another 1 h. Desorption curves were acquired under pure He atmosphere (30 mL/min) by heating the catalyst from 30 to 700 °C with a ramping rate of 10 $°C \cdot min^{-1}$. The CO or CO_2-TPD curve was recorded by mass spectra (MS, mass spectrometer LC-D200M, TILON) with $m/z = 28$ (N_2 or CO), 44 (CO_2), 2 (H_2), 18 (H_2O or NH_3), 14 (N) and 12 (C).

2.8. Mössbauer spectroscopy

The Mössbauer spectra (Analysis and Testing Center for Nuclear Science, Shanghai Institute of Applied Physics) were collected in a constant acceleration transmission mode with a 57 Co/Rh source at room temperature. The velocity was calibrated using 25 mm α-Fe foil, and the IS was calibrated to the center of α-Fe at room temperature.

2.9. X-ray absorption fine structure (XAFS)

For all the fresh and used catalysts, the *ex-situ* X-ray absorption fine structure (XAFS) spectra of Fe K-edge ($E_0 = 7112$ eV) were collected at BL14W1 beamline [40] of Shanghai Synchrotron Radiation Facility (SSRF), which was operated at 3.5 GeV under "top-up" mode with a constant current of 260 mA. All the XAFS data collection was performed under fluorescence mode and the energy was calibrated referred to the absorption edge of pure Fe foil. Athena and Artemis codes were used to extract the data and fit the profiles. The experimental absorption coefficients as a function of energies μ(E) were processed by background subtraction and normalization procedures for the X-ray absorption near edge structure (XANES) part and reported as "normalized absorption". Respectively, for the extended X-ray absorption fine structure (EXAFS) spectra, the Fourier transformed (FT) data in R space (the Fe—N/Fe—N—Fe or Fe—O/Fe—O—Fe shell) was analysed through using first-shell approximation or metallic Fe model. The passive electron factors (S_0^2) were confirmed by fixing the Fe—Fe coordination number (CN) to be 8 + 6 and fitting the experimental Fe foil data. After that, the data was fixed for further analysis of the measured samples. The other parameters were allowed to vary during the fit process, including that describing the electronic properties and local structure environment of bond distance (R), CN, and Debye–Waller factors (σ^2) around the absorbing atoms.

2.10. Catalytic test

The Fischer-Tropsch synthesis reaction tests were conducted using a fixed-bed flow reactor with an inner diameter of 10 mm under industrially relevant operation conditions. For all catalysts, 0.2 g sieved catalysts diluted with 0.3 g SiO_2 particles (40–60 mesh) were tested at FTS reaction condition (T = 280 °C, P = 20 bar, 47%CO/47%H_2/6%N_2, F = 30 mL/min). The catalytic measurements of Fe_2N/Al_2O_3 and bulk Fe_2N at different temperatures were carried out without any pre-treatment. In contrast, for the Fe_2O_3/Al_2O_3-IM/SG samples, both catalysts were reduced under 10%H_2/Ar feed ($F = 50$ mL/min) at 380 °C for 3 h, then tested at the same condition of iron nitrides mentioned above. To monitor the influence of structure transformation of iron nitride for FTS reaction, the catalytic behaviour of Fe_2N/Al_2O_3 was further valued at 20 bar, 330 °C, a gas mixture of 47%CO/47%H_2/6%N_2, and flow rate (F) of 30 mL/min. The reaction time was controlled with time-on-stream of 2 h, 10 h, 80 h, and 160 h.

The products and reactants in the gas phase were detected online using two tandem gas chromatography (Ouhua GC-9160). All the equipment and gas channels were kept at 250 °C. C_1—C_4 ranged hydrocarbons were analysed using a Plot Al_2O_3 capillary column with a flame ionization detector (FID); CO, CO_2, CH_4, and N_2 were analysed by using a Porapak Q and 5A molecule sieve-packed column with a thermal conductivity detector (TCD). During gas-phase product analysis, the N desorption of iron nitride was proved in the form of ammonia rather than N_2 molecule, and hence the N_2 here was used as the internal standard without interference. The selectivity of the products was all on

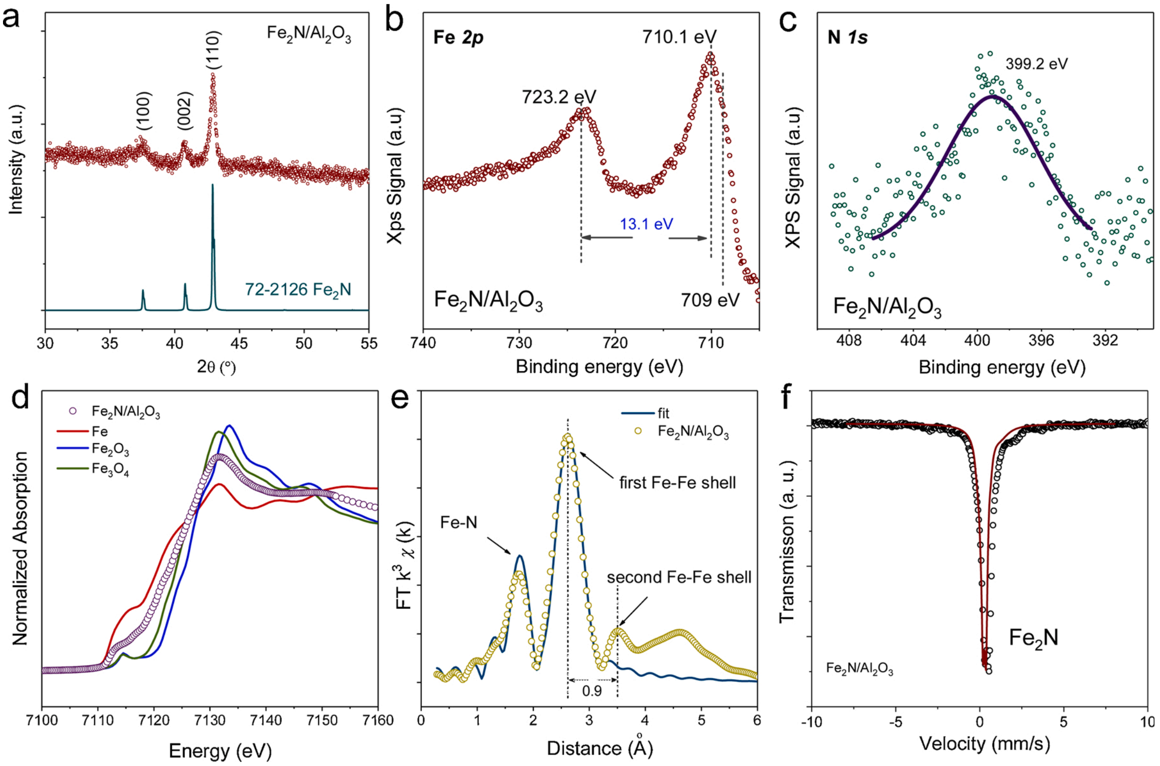

Fig. 2. Structural investigation of Fe_2N/Al_2O_3-fresh. (**a**) XRD pattern, (**b**) Fe 2*p* XPS spectrum, (c) N 1s XPS spectrum, (**d**) XANES spectra, (**e**) EXAFS spectra and (**f**) ^{57}Fe Mössbauer spectrum of as-prepared Fe_2N/Al_2O_3-fresh.

a carbon basis. For CO_2 selectivity, it was calculated basing on the all used CO and the selectivity of CH_4, C_2—C_4 and C_{5+} were based on all produced hydrocarbons excluding CO_2. All samples after FTS reaction were passivated by 1%O_2/Ar at room temperature and then quickly transferred to vials filled with N_2 gas for the goal of minimizing the possible re-oxidation of used catalysts for further structural characterizations (XRD, XAFS and XPS).

2.11. Calculations of CO adsorption on Fe_2N and Fe_3O_4

All spin-polarized calculations were performed using DMol^3 program. The first-principles calculations based on density functional theory were investigated to confirm the surface structures of Fe_2N and Fe_3O_4, as well as the adsorption sites for CO. Basing on generalized gradient approximations (GGA), the Perdew Burke Ernzerh of functional (PBE) [41] was adopted, and in addition, the TS method [42] for DFT-D correction was an implement that use to amend the adsorption energies. For acquiring dependable results, the convergence threshold of SCF iterations was set to 1.0×10^{-6} Hartree, the areas of cleaved surfaces were configured more than 8.0×8.0 Å^2, the thickness of vacuum slabs was 15.0 Å, and the Monkhorst-Pack k-point separation was specified to 0.04 Å^{-1}.)

3. Results and discussion

3.1. Fabrication of supported Fe_2N nanoparticles precursor

By using the iron oxides on alumina matrix (Fig. S1) as initial precursors, the supported iron nitride (Fe_2N) nanoparticles were prepared through a nitridation process under ammonia flow. The detailed preparation process is available experimental method part. As the nitrogen in metal nitrides has poor soundness and it will be spilled out crystal lattice at low NH_3 partial pressure, it is especially crucial to control the ratio of ammonia/hydrogen during nitridation process. The decrease in nitrogen content would result in a shrink of lattice parameters, as proved by the XRD patterns (Fig. S2). Therefore, by efficiently inhibiting the denitrification trend from Fe_2N to Fe_xN ($x > 2$), the phase-pure Fe_2N nanoparticles supported on mesoporous Al_2O_3 were controllably prepared.

As shown in the TEM and HAADF-STEM images (Figs. 1a, b, S3 and S4), these as-prepared Fe_2N particles with diameter of 28 ± 8 nm were dispersed on the mesoporous alumina support. Fig. 1c shows TEM image of an isolated Fe_2N nanoparticle on Al_2O_3 matrix. The two different structures revealed in figure emphasize that there is an amorphous layer coating on the out-surface of nanoparticles. By aids of AC-STEM-EELS and elemental mapping analysis in the same region (Figs. 1d and S3c), we found Fe and N located in the core domains, while O and Al were only observed in the outside region, which suggested the presence of core-shell structure for as-prepared Fe_2N/Al_2O_3 catalyst. The lattice spacing in selected area of the core (dash box, Fig. 1d) are 0.211 and 0.222 nm, corresponding to the distance of (011) and (002) plane of Fe_2N (Fig. 1e) respectively. In the XRD patterns shown in Fig. 2a, all the diffracted peaks are attributed to Fe_2N (JCPDS card no: 72-2126), implying the high purity of as formed Fe_2N phase. From the Fe XPS *2p* spectrum (Fig. 2b), the binding energy gap between Fe $2p_{1/2}$ *and* Fe $2p_{3/2}$ is 13.1 eV, which is obviously lower than that of iron oxide (13.6 eV, Fig. S5a) [43]. The absence of iron oxides in the outside layer is well in line with previous finding that the iron nitride demonstrates relatively superior resistance to oxidation [44,45]. Also, there is no detectable satellite peaks tagged for Fe_2O_3 or FeO species were observed. The XPS N 1s spectrum (Fig. 2c) centred at 399.2 eV revealed the nitrogen state of Fe—N [46], confirming the presence of the surface nitride. In addition, prominent shoulder peak is observed at 709.0 eV for catalyst, which is between 706.7 eV for metallic Fe and Fe $2p_{3/2}$ for FeO at 709.7 eV. This positive character of Fe_2N is well in line with the expectant results that the charge transfer from Fe to N atoms owing to the presence of Fe—N interaction [38]. In addition, dominant Fe $2p_{3/2}$ XPS signal was detected at relatively higher binding energy of 710.1 eV, proving the presence of interaction with the mesoporous Al_2O_3 in the outer layer. The averaged

Table 1
EXAFS fitting results of distance (*R*) and coordination number (CN) of the catalysts.

Sample	Fe—N/C		Fe—Fe		σ^2 (Å^2)	ΔE_0
	R (Å)	CN	*R* (Å)	CN		eV
Fe_2N/Al_2O_3-fresh	1.94 ± 0.02	2.9 ± 0.6	2.73 ± 0.02	4.2 ± 0.6	0.003 (N)	6.9 ± 3.1
Fe_2N/Al_2O_3-used	1.96 ± 0.04	2.4 ± 0.8	2.73 ± 0.04	2.0 ± 0.6	0.005 (Fe)	10.0 ± 6.3

electronic structure of as-prepared supported Fe_2N nanoparticles were further evaluated by XANES at Fe K-edge (Fig. 2d). Compared with Fe_3O_4 reference (green line), the shift of Fe pre-edge to lower energy indicates the electron-rich nature of Fe sites surrounded by N atoms in FeN structure, which is well in line with above XPS results. The electronic state of iron is mixed by Fe^0 and Fe^{2+}, and can be determined close to $Fe^{1.2+}$ by XANES liner combination analysis, which is similiar with predict of $Fe^{1.5+}$ basing on DFT calculation [38]. EXAFS data (Figs. 2e and S6) with the profile fit in *R* space were used to investigate the short-range local structure of FeN/Al_2O_3 catalysts. Comparing with metallic iron (2.50 Å), the iron atoms in hexagonal Fe_2N has a longer Fe—Fe coordination distance (2.76 Å) owing to the presence of N atoms in the surrounding interstitial position (Table 1). In the phase each Fe atom is surrounded by 6 interstitial positions in a *hcp* lattice, of which a maximum of 3 are occupied. The coordination number observed here (N = 2.9 ± 0.6) is close to the theoretical value, proving the pure phase nature of as prepared catalyst. ^{57}Fe Mössbauer spectroscopy is an effective characterization to determine and quantify the iron phases. As shown in Fig. 2f, the dominant presence of superparamagnetic Fe_2N is proved by the characteristic doublet, which is obviously different with the combination of sextets and doublets for Fe_3N or Fe_4N [47].

3.2. Catalytic performance of Fe_2N/Al_2O_3 catalyst

The supported Fe_2N nanoparticles was evaluated at 280 °C under a typical FTS reaction condition ($CO/H_2 = 1$, P = 20 bar) [29,48–50]. Two kinds of supported Fe_2O_3 nanoparticles catalysts were prepared and evaluated here as reference. Fe_2O_3/Al_2O_3-IM catalyst was prepared with the same impregnation method (Fig. S1) without further nitridation step; the other Fe_2O_3/Al_2O_3-SG catalyst was prepared by sol-gel method (Figs. S7 and S8). Remarkably, the conversion activity of as-prepared Fe_2N/Al_2O_3 displayed about 3 times higher than traditional reduced Fe_2O_3/Al_2O_3 catalysts (33 *vs.* 10–14 $\mu mol \cdot g_{Fe}^{-1} \cdot s^{-1}$, Fig. 3a and Table S1). To decrease the influence of reduction degree, the temperature or reduction time of H_2 pre-treatment for Fe_2O_3/Al_2O_3 catalysts were correspondingly increased (Figure S9). However, the Fe_2N/Al_2O_3 catalyst still obviously outperformed the reduced oxides catalysts even after slow carbonization process. In addition, comparing with the reduced oxides catalysts, superior selectivity of valuable hydrocarbons is achieved for Fe_2N/Al_2O_3 catalyst. The selectivity for desired $C_{2=}$—$C_{4=}$ and C_{5+} (Fig. 3b) is ~75 wt.% basing on total hydrocarbons over Fe_2N/Al_2O_3 catalyst, which is in accordance with its higher chain-growth probability as compared with reference catalysts (Fig. S10). Meanwhile, the selectivity of undesirable CO_2 is as low as ~20 %, which might be benefited from its stronger CO_2 adsorption ability as confirmed by CO_2-TPD results (Fig. S11). The catalytic performance in CO_2 selectivity for Fe_2N/Al_2O_3 is well in line with previous findings over Fe_2C catalysts [23]. Generally, the total selectivity of valuable products ($C_{2=}$—$C_{4=}$ and C_{5+}) basing on converted CO over Fe_2N/Al_2O_3 is as high as 60 wt.%, which is comparable with that of phase-pure Fe_5C_2 catalyst [19] and much better than assistant-free iron catalysts (see Table S1).

To be noted, for both kinds of reduced Fe_2O_3/Al_2O_3 catalysts, similar trends of gradual growth in FTS activity are observed in initial 20 h, indicating the presence of slow carburization progress under reaction condition. However, the Fe_2N/Al_2O_3 performs highly initial activity, confirming the intrinsically active feature of Fe atoms in the Fe_2N phase. Correspondingly, similar evolution in FTS activity was also observed over as-prepared Fe_5C_2 nanoparticles in previous report [19]. The degree of reduction (DOR) for reference oxides catalysts after pretreatment (Fe/Al_2O_3-IM and Fe/Al_2O_3-SG) are 44% and 49% (Fig. S12). To examine the degree of reduction (DOR) on the phase transformation over Fe based catalysts, the metallic iron as the initial phase should be investigated. However, basing on the in-situ structural monitor (Fig. S13), the metallic iron is difficult to be generated *via* the reduction of Fe_2O_3/Al_2O_3 catalysts owing to the formation of $Fe(AlO_4)_2$ under high reduction temperature by traditional ways. Therefore, according to the H_2-TPR profile of Fe_2N/Al_2O_3 (Fig. S14a), we conducted denitrification treatment under H_2 atmosphere over the as-prepared Fe_2N/Al_2O_3 catalyst at 500 °C. After denitrification pretreatment, only diffraction peaks of metallic iron are detectable in the XRD patterns (Fig. S14b). As shown in the Fig. S15, the catalytic performance of metallic iron precursor is obviously inferior in the CO conversion as comparing with Fe_2N/Al_2O_3 catalyst. In addition, one gradual induction period is observed in the first 20 h for the metallic iron catalyst, which is similar with the oxides precursor. These results support the deduction that DOR is not the determining factor in phase transformation of iron-based catalyst in this work. With the aim of studying contributions of various iron species, great efforts have been made to directly synthesis active structure and investigate its structure-function relationship [17,21,22,51]. Therefore, the evolution of catalytic performance upon

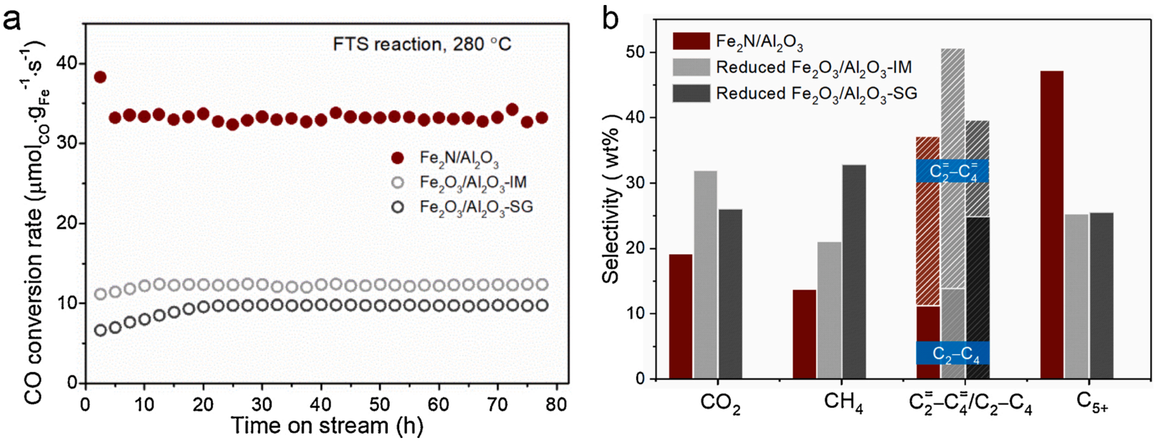

Fig. 3. Catalytic performance the Fe_2N/Al_2O_3 and reference catalysts. (**a**) Reactivity of CO hydrogenation and (**b**) product selectivity. The CH_4, C_2—C_4 and C_{5+} selectivity was calculated based on all hydrocarbons excluding CO_2. Reaction condition: $T = 280$ °C, $H_2/CO = 1:1$, $P = 20$ bar, $F = 30$ mL·min^{-1}, $W_{catal} = 0.2$ g.

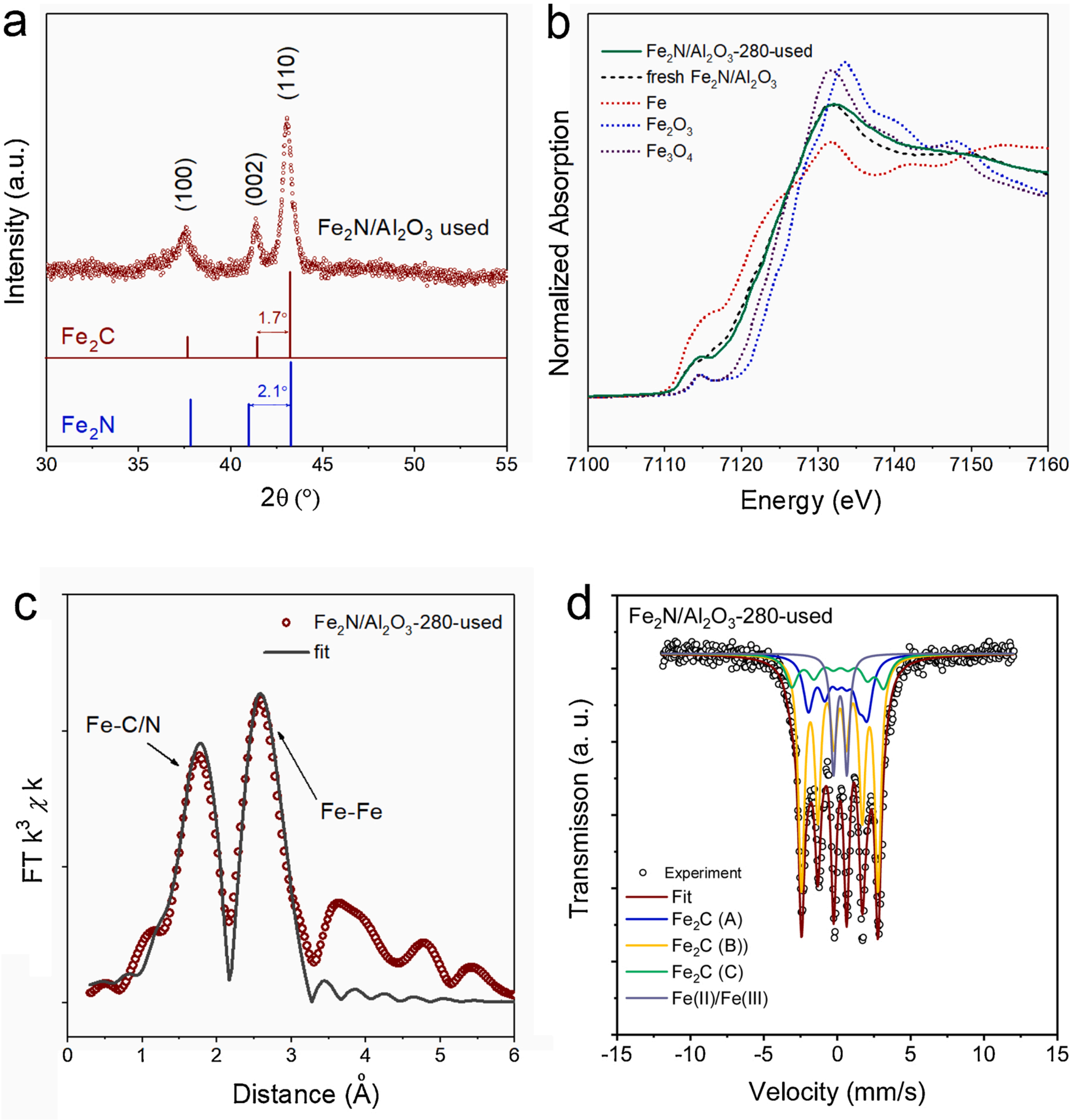

Fig. 4. Structural information of the used Fe_2N/Al_2O_3 catalyst after FTS reaction at 280 °C for 80 h. (**a**) XRD pattern, (**b**) XANES spectra, (**c**) EXAFS spectra and (**d**) ^{57}Fe Mössbauer spectrum.

Fe_2N/Al_2O_3 catalyst deserves more attention in this work.

3.3. *Structural determination and evolution of Fe_2N/Al_2O_3 catalyst after FTS reaction*

The diffracted peak at about 40.7° indexed as (002) reflection for the fresh Fe_2N phase shifts to 41.5° after FTS reaction at 280 °C for 80 h (Fig. 4a), suggesting the occurrence of phase transformation during FTS reaction. Aside from the slight shift of diffracted peaks, the positional distance between the peaks of (002) and (101) also shrinks from 2.2° to 1.8°, which is ascribed to the characteristic distance of Fe_2C (JCPDS card no: 36-1249). In addition, N 1s XPS signal is negligible after 80 h FTS testing (Fig. S16) as well, indicating sufficient replacement of N atoms by C atoms coupling with forming Fe_2C under reaction condition. Support also can be derived from the elemental mapping results as shown in Fig. S17 that the dispersion of C coincides with that of Fe, and N is barely detectable. In addition, the particle size of as formed Fe_2C change little after FTS reaction at 280 °C as shown in Fig. S18.

Table 2
^{57}Fe Mössbauer parameters of the Fe_2N/Al_2O_3 after FTS reaction at 280 °C.

Entries	IS (mm s^{-1})	QS (mm s^{-1})	A (%)	Phase ascription
1	0.23	−0.27	20.02	Fe_2C (A)
2	0.23	−0.02	54.12	Fe_2C (B)
3	0.18	−0.20	14.21	Fe_2C (C)
4	0.25	0.91	11.65	Fe(II)/Fe(III)

A, relative spectral area; IS, Isomer shift (relative to α-Fe); QS, quadrupole shift for sextet or quadruple splitting for doublet.

To confirm the corollary, we conducted XAFS characterization to give overall electronic and structural information of spent catalysts. As illustrated by Fourier transforms of the k^3-weighted Fe K-edge EXAFS results (Fig. 4c and Table 1), dominated Fe—C coordination of the first Fe shell centred at 1.94 Å, as well as the strong scattering of Fe—Fe at longer distance of 2.73 Å are observed for spent Fe_2N/Al_2O_3, which are basically the same as that of fresh Fe_2N/Al_2O_3 catalyst. As XRD results has proven that Fe_2C is the dominate phase for spent catalysts, this

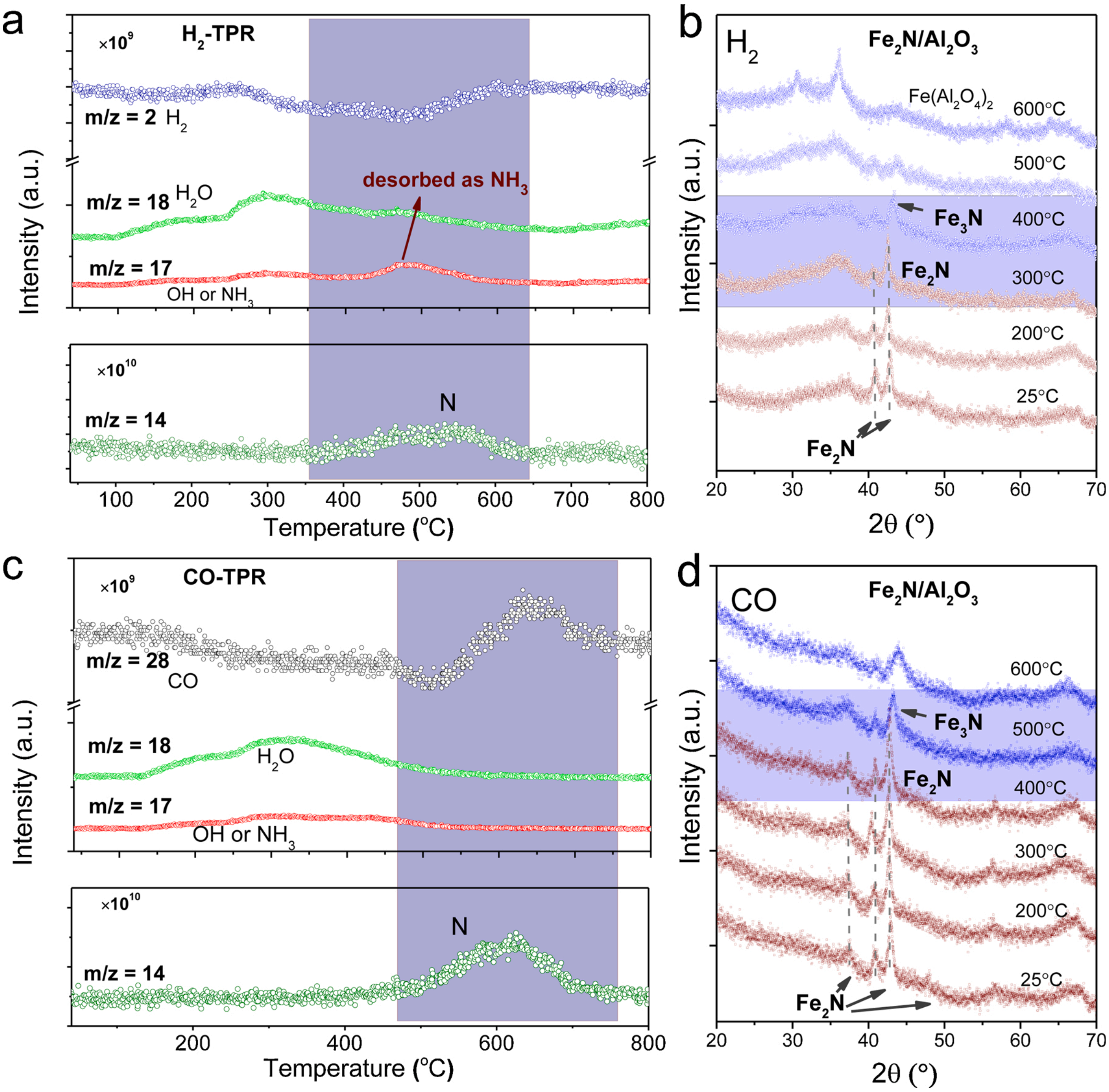

Fig. 5. Structural transformation of the Fe_2N/Al_2O_3 catalyst under different atmospheres. (**a**) H_2-TPR profile and (**b**) the corresponding *in-situ* XRD patterns; (**c**) CO-TPR profile of the Fe_2N/Al_2O_3 and (**d**) the corresponding *in-situ* XRD patterns. During both TPR measurements, the off-gas was monitored by mass spectrometer.

finding from EXAFS results indicates that the positions of interstitial N/C atoms in Fe_2N and Fe_2C are extremely close, which is well consistent with experimental [33] and computational results in former reports [38]. ^{57}Fe Mössbauer spectroscopy was used to clearly identify the phase components of Fe_2N/Al_2O_3 catalyst after FTS reaction. As revealed in Fig. 4d, the spectra of Fe_2N/Al_2O_3 collected after FTS reaction is deconvoluted with the corresponding parameters listed in Table 2. The presence of Fe_2C is evidenced by the combination of three sextets, which is ascribed to Fe_2C (A), Fe_2C (B) and Fe_2C (C) with different crystallographic positions in Fe_2C lattice [20]. The overall content of Fe_2C formed via Fe_2N intermedia after FTS reaction is as high as 88.4 % (Table 2). The superiority of Fe_2N/Al_2O_3 precursor in forming supported Fe_2C nanoparticles is also confirmed by poor carbonization of oxides iron (Fe_2O_3/Al_2O_3-IM and Fe_2O_3/Al_2O_3-SG catalysts) or metallic iron (Fe/Al_2O_3) after FTS reaction as shown in the ^{57}Fe Mössbauer spectroscopy (Figs. S19, S20 and Table S2).

After long-term reaction, the coordination number (CN) of Fe—C/N in the first shell is slightly decrease from 2.9 to 2.4, which might be stemmed from two potential reasons. On the one hand, it may be caused by the relative reduction in the number of interstitial atoms in the possible structure of Fe_2C. Another potential induction is that slight oxidation in the beginning of reaction decrease the averaged CN of Fe atoms, which might also be the origin to of slight deactivation from 38 to 33 $\mu mol \cdot g_{Fe}^{-1} \cdot s^{-1}$ in the first 2 h. Support can also be derived from the ^{57}Fe Mössbauer spectroscopy results that the presence of superparamagnetic doublet with the IS value of 0.25 $mm \cdot s^{-1}$ and the QS value of 0.91 $mm \cdot s^{-1}$ proves the generation of Fe(II)/Fe(III) species [52].

Notably, the electronic state of Fe atoms in the spent Fe_2N/Al_2O_3 catalyst determined by XANES is between Fe^0 and Fe^{2+}, close to $Fe^{1.0+}$ (Fig. 4b). Comparing with the fresh Fe_2N/Al_2O_3 catalyst (dash line), negligible change is observed in the pre-edge position of Fe atoms after FTS reaction. The resemble coordination structures of Fe_2N and Fe_2C achieve their comparably electronic property of Fe sites. As the catalytic activity during long-term test was roughly unchanged, it is reasonable that the iron atoms surrounded by interstitial N/C atoms are intrinsically active in catalysing CO hydrogenation reaction. Calculated results also confirm the electronic feature of surface iron atoms in the Fe_2N (+0.23 *vs.* + 0.76 eV for Fe_3O_4). Such property of surface contributes the formation of π back-bonding between adsorbed CO and surface iron atoms, which probably contribute to the superior catalytic performance finally. This finding is well consistent with stronger CO adsorption ability of

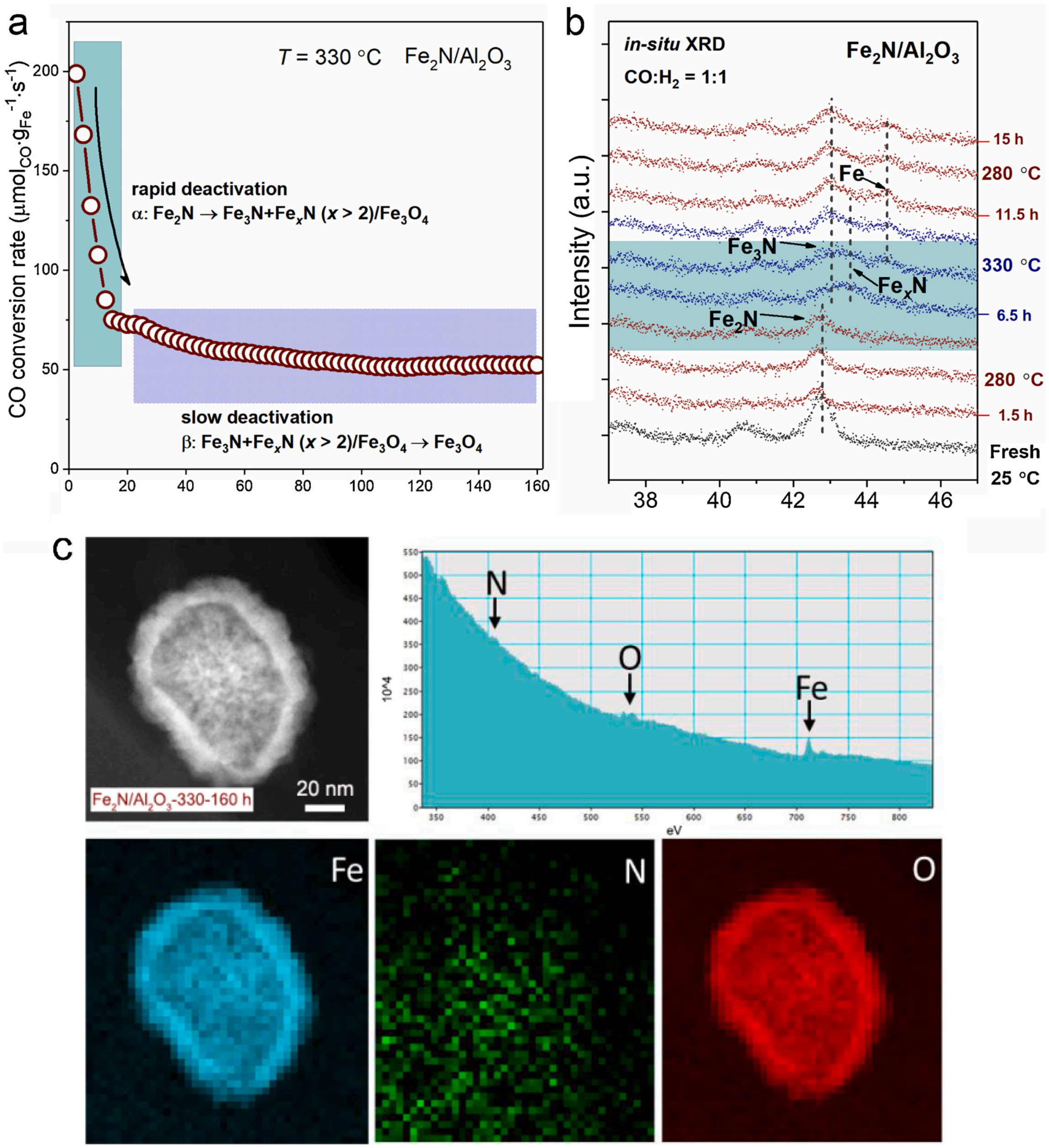

Fig. 6. Structural evolution at elevated temperature for Fe_2N/C catalysts. (**a**) Long-term FTS activity of the Fe_2N/Al_2O_3 catalyst at 330 °C for 160 h, reaction condition: $H_2/CO = 1:1$, P = 20 bar, F = 34 mL· min^{-1}, W = 0.2 g; (**b**) *In-situ* XRD patterns of the Fe_2N/Al_2O_3 collected under 50 %CO/H_2 feed, T: 25 °C → 280 °C → 330 °C → 280 °C. (**c**) HAADF-STEM image, the corresponding EELS spectrum and corresponding element mapping images of the Fe_2N/Al_2O_3 catalyst after FTS reaction for 160 h.

Fe_2N/Al_2O_3 catalyst as revealed in the CO-TPD profile, which is also confirmed by simulated DFT results (Figs. S21 and S22).

In order to discern the formation process of active Fe_2C species *via* Fe_2N precursor clearly, we conducted temperature programmed reduction tests (H_2-TPR and CO-TPR) and *in-situ* XRD to monitor the structural evolution of Fe_2N/Al_2O_3 catalyst. When the Fe_2N/Al_2O_3 is exposed to H_2 (Fig. 5a), small peak of N signal ($m/z = 14$, dark green) with one identical NH_3 evolution ($m/z = 17$, red) is observed in the range of 350–650 °C, revealing the N atoms in the Fe_2N escaped in the form of NH_3. In contrast, when Fe_2N/Al_2O_3 catalyst was exposed to CO feed (Fig. 5c), the desorption peak of N ($m/z = 14$) is observed at elevated temperature of 700 °C. In addition, correspondingly denitrified process is further confirmed by *in-situ* XRD results (Fig. 5b and d), that denitrification step is observed in the range of 300–400 °C under H_2 condition. In comparison, Fe_2N phase is still available as temperature increasing to 500 °C under CO atmosphere, proving that only CO molecules is insufficient to carburize Fe_2N at low temperature and ambient pressure. Moreover, as shown in the time-sequenced XRD results collected after FTS reaction (Fig. S23), the presence of denitrided Fe_3N and Fe_2C in the initial period also indicate the potential role of H_2 in phase transformation. In Fe_2N phase, all the Fe atoms are neighboured with 3 interstitial N atoms. As proved previously, the strong interstitial repulsion induced by the abundant Fe(3*I*) regions in Fe_2N can impede the N or C diffusion. [35] Combining the above results, the presence of H_2 molecules during reaction could play a role in promoting the transfer of interstitial N atoms. Subsequently, the transformation of N atoms might motivate the subsequent C infiltration into the crystal lattice with the formation of Fe_2C at relatively low temperatures, where the low temperature is indispensable to stabilize Fe_2C phase [30].

To further clarify the essential conditions for efficiently forming

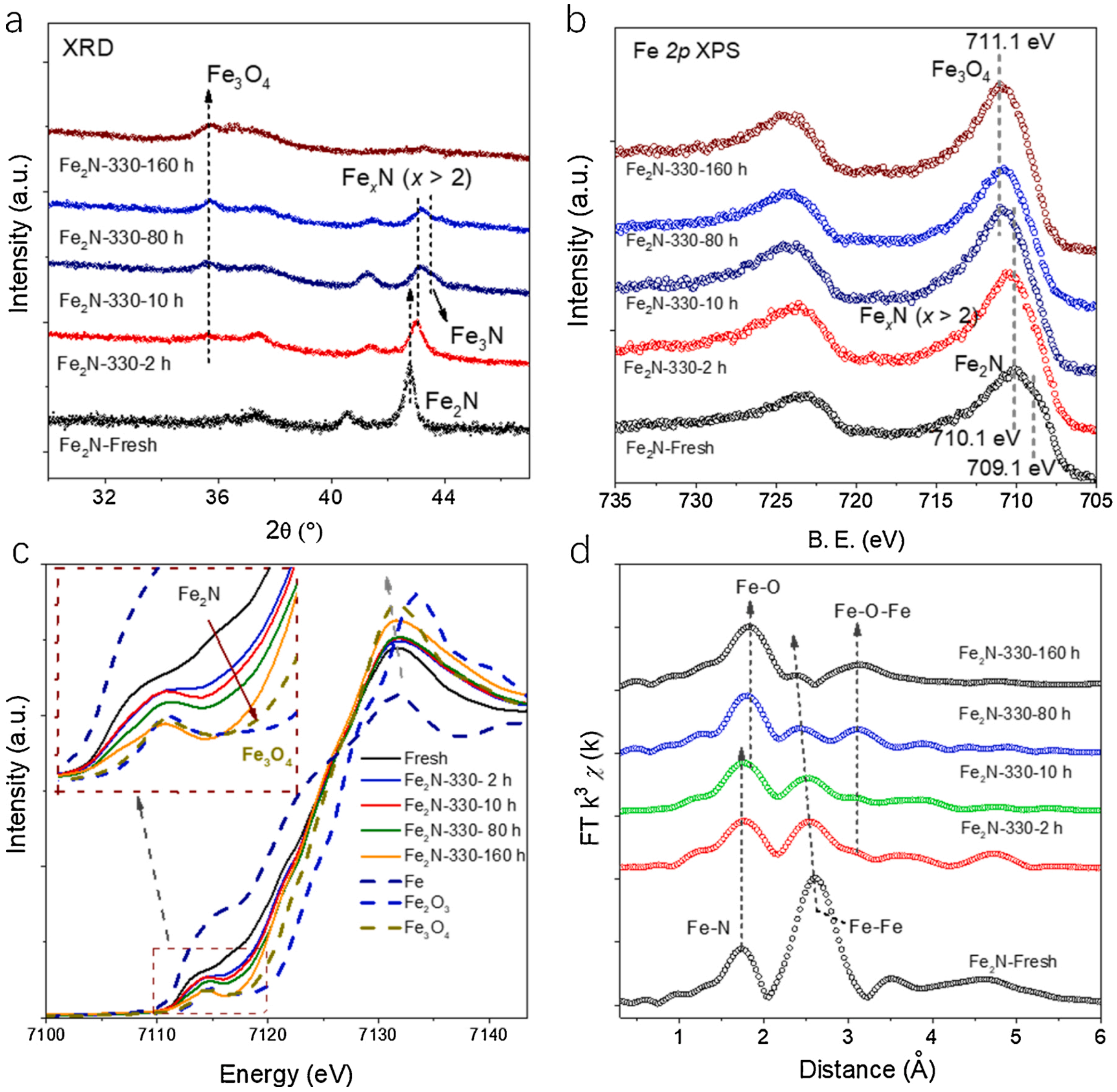

Fig. 7. Structural evolution of the Fe_2N/Al_2O_3 catalyst at different stages of FTS reaction at 330 °C. (**a**) XRD patterns, (**b**) Fe *2p* XPS spectra (**c**) XANES spectra and (**d**) EXAFS spectra.

Fe_2C/Al_2O_3, the activity evolution and corresponding structure changes of Fe_2C/Al_2O_3 media were monitored with elevated temperature (Fig. 6a). Generally, the deactivation of catalyst could be ascribed to the following three aspects: the active phase is converted to an inert phase; the deposition of carbonaceous material or coke; the loss of active surface area due to the sintering. As shown in Table 1, the selectivity of C_{5+} at 330 °C is slightly lower than that under 280 °C, indicating the relatively weak possibility that the active sites are covered by the high molecular waxes. Additionally, the CO conversion activity dramatically decreased at 330 °C in the initial stage, whereas the averaged size of nanoparticles changes little according to the statistical results (Fig. S24). Therefore, we can primarily estimate that the key factor for the deactivation here are not carbon deposition or sintering. On account of denitrification occurred at 300–400 °C in presence of H_2 as revealed by *in-situ* XRD results (Fig. 5b), the Fe_2N/Al_2O_3 catalyst was further valued at 330 °C under FTS reaction condition. As observed from the *in-situ* XRD patterns collected under ambient pressure (Fig. 6b), the crystal structure of Fe_2N phase is immediately destroyed as the temperature increasing up to 330 °C, which is consistent with the absence of N signal shown in the corresponding EELS spectrum of spent catalysts (Fig. 6c). These characterization results reveal that the fast collapse of Fe_2N structure in the initial stage during FTS reaction results in its failure in transforming into Fe_2C phase. Alternatively, the presence of interstitial N atoms is indispensable for the substitute of dissociated C atoms during FTS reaction at relatively low temperature of 280 °C.

Furthermore, spent catalysts were collected after various stages of the reaction at 330 °C (named as Fe_2N/Al_2O_3-330-*x*, *x* means the reaction time, where $x = 0, 2, 10, 80, 160$ h respectively). In detail, in initial α-stage (0–10 h), the lattice contraction as revealed in XRD patterns (Fig. 7a) indicates that the content of interstitial nitrogen in Fe_2N/Al_2O_3 is decreased [34], which is well matched with the decreasing Fe—Fe coordination observed from EXAFS results (Fig. 7d). The Fe_3N/Al_2O_3 was generated by further denitrification treatment under H_2 over Fe_2N/Al_2O_3. As shown in Fig. S25, the Fe_3N phase is dominantly present after hydrogen treatment according to the XRD patterns. As expected, the initial FTS activity of Fe_3N/Al_2O_3 is obviously lower than that of Fe_2N/Al_2O_3, proving the less active nature of Fe_3N phase. Additionally, surface Fe atoms of Fe_2N/Al_2O_3 catalyst is rapidly oxidized as clearly proved by XPS spectra (Fig. 7b), where the binding energy of Fe 2*p* shifted from 710.1 to 711.1 eV. At same time, the FTS activity steeply decrease from 200 to 75 $\mu mol \cdot g_{Fe} \cdot s^{-1}$ in the initial 10 h (Fig. 6a). At the following β-stage, one much slower structure evolution from Fe_3N

(C)/Fe_xN ($2 < x < 3$) to Fe_3O_4 is observed in the XRD, XPS and XAFS results (as shown in Fig. 7 and Table S3). The partial carburization of Fe_3N to Fe_3C might be included in this process as their extremely close structures. Time-sequenced TEM images (Fig. S26) also clearly reveal a gradual evolution from outside to inside, where the crystalized core of Fe_2N is gradually disordered during FTS reaction. During this stage, the FTS reactivity is slowly and slightly decreased from 75 to 50 μmol g_{Fe}^{-1} s^{-1}. On basis of that, we can conclude that the Fe atoms in Fe_3N(C)/Fe_xN ($2 < x < 3$) structure without sufficient surrounding N/C atoms are far less-active than Fe atoms in Fe_2N(C) structure with an electron-rich feature. Additionally, the absence of active Fe_2N(C) structure also induce a poor anti-oxidation capacity of iron species under reaction condition [35]. Moreover, as-formed Fe_2C also greatly outperformed metallic Fe catalysts prepared in comparable method in catalysing FTS reaction (Figs. S15 and S20). For one aspect, it was ascribed to the barely metallic Fe particles is weak in anti-oxidation in the presence of H_2O and CO_2 during FTS reaction, which the outside surface of iron particles is apt to become inactive iron oxides. And for another, metallic Fe atoms is weak to be carbonized in the absence of interstitial atoms, indicating the importance of starting material in Fe_2C formation.

4. Conclusion

By effectively inhibiting the denitrification, pure-phase Fe_2N nanoparticles supported on alumina were successfully prepared and evaluated as catalysts for FTS reaction. The carbides have long been predicted to be promising for FTS reaction previously. However, the kinetic barrier hindered the formation of Fe_2C through the directly carburation of metallic iron or iron oxides. Here, iron species are efficiently converted into highly active Fe_2C structures mediated by the Fe_2N as precursor during FTS reaction. As-formed Fe_2C supported nanoparticles exhibited promising catalytic performance at 280 °C, including good stability and high selectivity for desired hydrocarbons products. In addition, benefiting from the predominantly existing Fe_2C phase, we can clearly prove Fe_2C as an active site for FTS reaction, which might be determined by the electron-rich feature of Fe sites in the Fe_2X (N or C) structures. The role of Fe_2N precursor in this work can be attributed to two aspects: the coordination structure of Fe_2N achieve the electron-rich and highly active features of Fe atoms; the pre-existing N atoms effectually lower the barrier to form active Fe_2C phase. These findings broaden the approach to fabricate Fe_2C catalysts and deepen the understanding of its active nature and structure-reactivity relation during FTS reaction.

Author contributions

C.-J. Jia, R. Si, and C.-H. Yan supervised the work; X.-P. Fu, R. Si, and C.-J. Jia had the idea for and designed the experiments, analysed the results and wrote the manuscript; C. Ma performed the HRTEM and EELS measurements; X.-P. Fu, P.-N. Ren, F.-Y. Jia and M-Y, Li performed the catalyst preparation; X.-P. Fu and W.-Z. Yu performed the catalytic tests, chemical adsorption experiments; Jun-Lin and Shi-Qi Sun performed the Mössbauer spectroscopy characterization and analysis the results; X.-P. Fu and W.-W. Wang performed the *ex-situ/in-situ* XRD measurements; R. Si and X. Wang performed the XAFS measurements and analysed the results; K. Wu and C.-H. Yan conducted the XPS tests; S.-Q. Li performed the calculations of CO adsorption.

Declaration of Competing Interest

The authors report no declarations of interest.

Acknowledgments

Financial supported from the Excellent Young Scientists Fund from NSFC (21622106), the National Science Foundation of China (NSFC) (grant nos. 21771117</GN3>, <GN2>21331001, 21773288 and 11574281), the Outstanding Scholar Fund (grant no. JQ201703) and the Doctoral Fund (grant no. ZR2018BB010) from the Science Foundation of Shandong Province of China, the Taishan Scholar project of Shandong Province of China. We thank the Center of Structural Characterization and Property Measurements at Shandong University for the help on sample characterizations.

Appendix A. Supplementary data

Supplementary material related to this article can be found, in the online version, at doi:https://doi.org/10.1016/j.apcatb.2020.119702.

References

[1] K. Keyvanloo, M.K. Mardkhe, T.M. Alam, C.H. Bartholomew, B.F. Woodfield, W. C. Hecker, Supported iron Fischer-Tropsch catalyst: superior activity and stability using a thermally stable silica-doped alumina support, ACS Catal. 4 (2014) 1071–1077.

[2] R. Zhang, L. Kang, H. Liu, B. Wang, D. Li, M. Fan, Crystal facet dependence of carbon chain growth mechanism over the hcp and fcc Co catalysts in the Fischer-Tropsch synthesis, Appl. Catal. B: Environ. 269 (2020), 118847.

[3] A.Y. Khodakov, W. Chu, P. Fongarland, Advances in the development of novel cobalt Fischer-Tropsch catalysts for synthesis of long-chain hydrocarbons and clean fuels, Chem. Rev. 107 (2007) 1692–1744.

[4] L. Zhong, F. Yu, Y. An, Y. Zhao, Y. Sun, Z. Li, T. Lin, Y. Lin, X. Qi, Y. Dai, L. Gu, J. Hu, S. Jin, Q. Shen, H. Wang, Cobalt carbide nanoprisms for direct production of lower olefins from syngas, Nature 538 (2016) 84–87.

[5] F. Jiao, J. Li, X. Pan, J. Xiao, H. Li, H. Ma, M. Wei, Y. Pan, Z. Zhou, M. Li, S. Miao, J. Li, Y. Zhu, D. Xiao, T. He, J. Yang, F. Qi, Q. Fu, X. Bao, Selective conversion of syngas to light olefins, Science 351 (2016) 1065–1068.

[6] R. Luque, A.R. de la Osa, J.M. Campelo, A.A. Romero, J.L. Valverde, P. Sanchez, Design and development of catalysts for biomass-to-liquid-Fischer-Tropsch (btl-FT) processes for biofuels production, Energy Environ. Sci. 5 (2012) 5186–5202.

[7] X. Fu, Q. Shen, D. Shi, K. Wu, Z. Jin, X. Wang, R. Si, Q. Song, C. Jia, C. Yan, Co_3O_4-Al_2O_3 mesoporous hollow spheres as efficient catalyst for Fischer-Tropsch synthesis, Appl. Catal. B: Environ. 211 (2017) 176–187.

[8] P. Zhai, C. Xu, R. Gao, X. Liu, M. Li, W. Li, X. Fu, C. Jia, J. Xie, M. Zhao, X. Wang, Y. Li, Q. Zhang, X. Wen, D. Ma, Highly tunable selectivity for syngas-derived alkenes over zinc and sodium-modulated Fe_5C_2 catalyst, Angew. Chem. Int. Ed. 55 (2016) 9902–9907.

[9] K. Cheng, B. Gu, X. Liu, J. Kang, Q. Zhang, Y. Wang, Direct and highly selective conversion of synthesis gas into lower olefins: design of a bifunctional catalyst combining methanol synthesis and carbon-carbon coupling, Angew. Chem. Int. Ed. 128 (2016) 4803–4806.

[10] P.R. Ellis, D.I. Enache, D.W. James, D.S. Jones, G.J. Kelly, A robust and precious metal-free high performance cobalt Fischer-Tropsch catalyst, Nat. Catal. 2 (2019) 623–631.

[11] W. Li, J. Liu, J. Gu, W. Zhou, S. Yao, R. Si, Y. Guo, H. Su, C. Yan, W. Li, Y. Zhang, D. Ma, Chemical insights into the design and development of face-centered cubic ruthenium catalysts for Fischer-Tropsch synthesis, J. Am. Chem. Soc. 139 (2017) 2267–2276.

[12] T.A. Wezendonk, V.P. Santos, M.A. Nasalevich, Q.S.E. Warringa, A.I. Dugulan, A. Chojecki, A.C.J. Koeken, M. Ruitenbeek, G. Meima, H. Islam, G. Sankar, M. Makkee, F. Kapteijn, J. Gascon, Elucidating the nature of Fe species during pyrolysis of the Fe-BTC MOF into highly active and stable Fischer-Tropsch catalysts, ACS Catal. 6 (2016) 3236–3247.

[13] J. Bae, S.Y. Hong, J.C. Park, G.B. Rhim, M.H. Youn, H. Jeong, S.W. Kang, J. Yang, H. Jung, D.H. Chun, Eco-friendly prepared iron-ore-based catalysts for Fischer-Tropsch synthesis, Appl. Catal. B: Environ. 244 (2019) 576–582.

[14] Z. Yang, S. Guo, X. Pan, J. Wang, X. Bao, FeN nanoparticles confined in carbon nanotubes for CO hydrogenation, Energy Environ. Sci. 4 (2011) 4500.

[15] H.M. Torres Galvis, J.H. Bitter, C.B. Khare, M. Ruitenbeek, A.I. Dugulan, K.P. de Jong, Supported iron nanoparticles as catalysts for sustainable production of lower olefins, Science 335 (2012) 835–838.

[16] G. Yu, B. Sun, Y. Pei, S. Xie, S. Yan, M. Qiao, K. Fan, X. Zhang, B. Zong, Fe_xO_y@C spheres as an excellent catalyst for Fischer-Tropsch synthesis, J. Am. Chem. Soc. 132 (2010) 935–937.

[17] S. Kang, J.W. Bae, J. Cheon, Y. Lee, K. Ha, K. Jun, D. Lee, B. Kim, Catalytic performance on iron-based Fischer-Tropsch catalyst in fixed-bed and bubbling fluidized-bed reactor, Appl. Catal. B: Environ. 103 (2011) 169–180.

[18] B. An, K. Cheng, C. Wang, Y. Wang, W. Lin, Pyrolysis of metal-organic frameworks to Fe_3O_4@Fe_5C_2 core–shell nanoparticles for Fischer-Tropsch synthesis, ACS Catal. 6 (2016) 3610–3618.

[19] C. Yang, H. Zhao, Y. Hou, D. Ma, Fe_5C_2 nanoparticles: a facile bromide-induced synthesis and as an active phase for Fischer-Tropsch synthesis, J. Am. Chem. Soc. 134 (2012) 15814–15821.

[20] K. Xu, B. Sun, J. Lin, W. Wen, Y. Pei, S. Yan, M. Qiao, X. Zhang, B. Zong, ε-Iron carbide as a low-temperature Fischer-Tropsch synthesis catalyst, Nat. Commun. 5 (2014) 5783, https://doi.org/10.1038/ncomms6783.

[21] S. Janbroers, P.A. Crozier, H.W. Zandbergen, P.J. Kooyman, A model study on the carburization process of iron-based Fischer-Tropsch catalysts using in situ TEM-EELS, Appl. Catal. B: Environ. 102 (2011) 521–527.

[22] Q. Chang, C. Zhang, C. Liu, Y. Wei, A.V. Cheruvathur, A.I. Dugulan, J. W. Niemantsverdriet, X. Liu, Y. He, M. Qing, L. Zheng, Y. Yun, Y. Yang, Y. Li, Relationship between iron carbide phases (ε-Fe_2C, Fe_7C_3, and χ-Fe_5C_2) and catalytic performances of Fe/SiO_2 Fischer-Tropsch catalysts, ACS Catal. 8 (2018) 3304–3316.

[23] P. Wang, W. Chen, F.K. Chiang, A.I. Dugulan, Y. Song, R. Pestman, K. Zhang, J. Yao, B. Feng, P. Miao, W. Xu, E. Hensen, Synthesis of stable and low-CO_2 selective epsilon-iron carbide Fischer-Tropsch catalysts, Sci. Adv. 4 (2018) u2947.

[24] C. Yang, B. Zhao, R. Gao, S. Yao, P. Zhai, S. Li, J. Yu, Y. Hou, D. Ma, Construction of synergistic Fe_5C_2/Co heterostructured nanoparticles as an enhanced low temperature Fischer-Tropsch synthesis catalyst, ACS Catal. 7 (2017) 5661–5667.

[25] M.D. Shroff, D.S. Kalakkad, K.E. Coulter, S.D. Kohler, M.S. Harrington, N. B. Jackson, A.G. Sault, A.K. Datye, Activation of precipitated iron Fischer-Tropsch synthesis catalysts, J. Catal. 156 (1995) 185–207.

[26] E. de Smit, B.M. Weckhuysen, The renaissance of iron-based Fischer-Tropsch synthesis: on the multifaceted catalyst deactivation behavior, Chem. Soc. Rev. 37 (2008) 2758.

[27] A. Königer, C. Hammerl, M. Zeitler, B. Rauschenbach, Formation of metastable iron carbide phases after high-fluence carbon ion implantation into iron at low temperatures, Phys. Rev. B 55 (1997) 8143–8147.

[28] T. Herranz, S. Rojas, F. Perezalonso, M. Ojeda, P. Terreros, J. Fierro, Genesis of iron carbides and their role in the synthesis of hydrocarbons from synthesis gas, J. Catal. 243 (2006) 199–211.

[29] V.P. Santos, T.A. Wezendonk, J.J.D. Jaén, A.I. Dugulan, M.A. Nasalevich, H. Islam, A. Chojecki, S. Sartipi, X. Sun, A.A. Hakeem, A.C.J. Koeken, M. Ruitenbeek, T. Davidian, G.R. Meima, G. Sankar, F. Kapteijn, M. Makkee, J. Gascon, Metal organic framework-mediated synthesis of highly active and stable Fischer-Tropsch catalysts, Nat. Commun. 6 (6) (2015) 6451, https://doi.org/10.1038/ncomms7451.

[30] E. de Smit, F. Cinquini, A.M. Beale, O.V. Safonova, W. van Beek, P. Sautet, B. M. Weckhuysen, Stability and reactivity of ε-χ-θ iron carbide catalyst phases in Fischer-Tropsch synthesis: controlling μ_c, J. Am. Chem. Soc. 132 (2010) 14928–14941.

[31] X. Yu, X. Zhang, Y. Meng, Y. Zhao, Y. Li, W. Xu, Z. Liu, CO adsorption, dissociation and coupling formation mechanisms on Fe_2C(001) surface, Appl. Surf. Sci. 434 (2018) 464–472.

[32] X. Teng, S. Huang, J. Wang, H. Wang, Q. Zhao, Y. Yuan, X. Ma, Fabrication of Fe_2C embedded in hollow carbon spheres: a high-performance and stable catalyst for Fischer-Tropsch synthesis, ChemCatChem 10 (2018) 3883–3891.

[33] R.B. Anderson, J.F. Shultz, B. Seligman, W.K. Hall, H.H. Storch, Studies of the Fischer-Tropsch synthesis. Vii. Nitrides of iron as catalysts, J. Am. Chem. Soc. 72 (1950) 3502–3508.

[34] R.B. Anderson, Iron nitrides as Fischer-Tropsch catalysts, Adv. Catal 5 (1953) 355–384.

[35] E. Yeh, N.K. Jaggi, J.B. Butt, L.H. Schwartz, Silica-supported iron nitride in Fischer-Tropsch reactions: i. Characterization of the catalyst, J. Catal. 91 (1985) 231–240.

[36] E. Yeh, L.H. Schwartz, J.B. Butt, Silica-supported iron nitride in Fischer-Tropsch reactions: ii. Comparison of the promotion effects of potassium and nitrogen on activity and selectivity, J. Catal. 91 (1985) 241–253.

[37] A.A. Hummel, A.P. Wilson, W.N. Delgass, Surface and bulk changes in iron nitride catalysts in H_2/CO mixtures, J. Catal. 113 (1988) 236–249.

[38] C.M. Fang, M.A. van Huis, J. Jansen, H.W. Zandbergen, Role of carbon and nitrogen in Fe_2C and Fe_2N from first-principles calculations, Phys. Rev. B 84 (2011) 94102.

[39] T. Liapina, A. Leineweber, E.J. Mittemeijer, W. Kockelmann, The lattice parameters of ε-iron nitrides: lattice strains due to a varying degree of nitrogen ordering, Acta Mater. 52 (2004) 173–180.

[40] H.S. Yu, X. Wei, J. Li, S. Gu, S. Zhang, L. Wang, J. Ma, L. Li, Q. Gao, R. Si, F. Sun, Y. Wang, F. Song, H. Xu, X. Yu, Y. Zou, J. Wang, Z. Jiang, Y. Huang, The XAFS beamline of SSRF, Nucl. Sci. Tech. 26 (2015) 4–10.

[41] J.P. Perdew, K.E. Burke, Generalized gradient approximation made simple, Phys. Rev. Lett. 77 (1996) 3865, https://doi.org/10.1103/PhysRevLett.77.3865.

[42] A. Tkatchenko, M. Scheffler, Accurate molecular van der Waals interactions from ground-state electron density and free-atom reference data, Phys. Rev. Lett. 102 (2009) 73005.

[43] T. Yamashita, P. Hayes, Analysis of XPS spectra of Fe^{2+} and Fe^{3+} ions in oxide materials, Appl. Surf. Sci. 254 (2008) 2441–2449.

[44] R.B. Anderson, Nitrided iron catalysts for the Fischer-Tropsch synthesis in the eighties, Catal. Rev. 21 (1980) 53–71.

[45] Z. Yang, X. Pan, J. Wang, X. Bao, FeN particles confined inside CNT for light olefin synthesis from syngas: effects of Mn and K additives, Catal. Today 186 (2012) 121–127.

[46] M. Balogun, M. Yu, Y. Huang, C. Li, P. Fang, Y. Liu, X. Lu, Y. Tong, Binder-free Fe_2N nanoparticles on carbon textile with high power density as novel anode for high-performance flexible lithium ion batteries, Nano Energy 11 (2015) 348–355.

[47] L. Li, M. Qing, X. Liu, H. Wang, S. Liu, Y. Zhang, H. Wan, X. Wen, Y. Yang, Y. Li, Efficient one-pot synthesis of higher alcohols from syngas catalyzed by iron nitrides, ChemCatChem (2020) 1939–1943.

[48] R.P. Mogorosi, N. Fischer, M. Claeys, E. van Steen, Strong-metal-support interaction by molecular design: Fe-silicate interactions in Fischer-Tropsch catalysts, J. Catal. 289 (2012) 140–150.

[49] Q. Cheng, N. Zhao, S. Lyu, Y. Tian, F. Gao, L. Dong, Z. Jiang, J. Zhang, N. Tsubaki, X. Li, Tuning interaction between cobalt catalysts and nitrogen dopants in carbon nanospheres to promote Fischer-Tropsch synthesis, Appl. Catal. B: Environ. 248 (2019) 73–83.

[50] J. Li, Y. He, L. Tan, P. Zhang, X. Peng, A. Oruganti, G. Yang, H. Abe, Y. Wang, N. Tsubaki, Integrated tuneable synthesis of liquid fuels via Fischer-Tropsch technology, Nat. Catal. 1 (2018) 787–793.

[51] S. Mazzucco, Y. Wang, M. Tanase, M. Picher, K. Li, Z. Wu, S. Irle, R. Sharma, Direct evidence of active and inactive phases of Fe catalyst nanoparticles for carbon nanotube formation, J. Catal. 319 (2014) 54–60.

[52] G. Li, J. Smith, H. Inomata, Synthesis of nanoscale $Ce_{1\text{-}x}Fe_xO_2$ solid solutions via a low-temperature approach [14], J. Am. Chem. Soc. 123 (2001) 11091–11092.